arXiv:cond-mat/0201426v1 [cond-mat.mtrl-sci] 23 Jan 2002

Atomistic Studies of Defect Nucleation during Nanoindentation of Au (001)

Anil Gannepalli and Surya K. Mallapragada*
Department of Chemical Engineering, Iowa State University
Ames, Iowa 50011-2230
(Dated: March 22, 2022)

Atomistic studies are carried out to investigate the formation and evolution of defects during nanoindentation of a gold crystal. The results in this theoretical study complement the experimental investigations [J. D. Kiely and J. E. Houston, Phys. Rev. B **57**, 12588 (1998)] extremely well. The defects are produced by a three step mechanism involving nucleation, glide and reaction of Shockley partials on the {111} slip planes noncoplanar with the indented surface. We have observed that slip is in the directions along which the resolved shear stress has reached the critical value of approximately 2 GPa. The first yield occurs when the shear stresses reach this critical value on all the {111} planes involved in the formation of the defect. The phenomenon of strain hardening is observed due to the sessile stair-rods produced by the zipping of the partials. The dislocation locks produced during the second yield give rise to permanent deformation after retraction.

PACS numbers: 62.20.Fe, 62.20.Qp

I. INTRODUCTION

Understanding the detailed mechanics of material deformation is a fundamental challenge in materials science. In metals, the defect structures produced during deformation influence the material properties and behavior critically.[1,2] The formation and evolution of such structures have their basis in atomistic processes and the study of these nanoscale phenomena is paramount to the understanding of macroscopic phenomena such as fracture, friction, strain hardening and adhesion. The results of such research will also greatly facilitate the design of novel materials with desired properties. These insights into material behavior can be exploited to create desired dislocation patterns which can then be etched in a controlled manner to fabricate nanopatterns and nanostructures.[3]

Nanoindentation experiments, with the advent of scanning probe microscopes and advances in indentation techniques, are capable of experimentally probing material properties and phenomena at the nanoscale.[4,5,6] At these atomic length scales, the continuum models of deformation do not perform well and atomistic methods need to be considered to investigate the nanoscale deformation behavior. Advances in computational capability and high performance techniques have enabled researchers to investigate nanoindentation studies of comparable length scales theoretically using molecular dynamics simulations.[7,8] The experiments, for most part, have emphasized quantitative investigation of mechanical properties by measuring the force displacement curves, and the theoretical computer simulations have been targeted at studying the atomistic processes involved in plastic deformation during indentation experiments. The primary goal of such studies is to complement the experimental findings with theoretical investigations in understanding the mechanisms of plastic deformation in materials.

In this paper, we present results of atomistic studies of nanoindentation of a passivated gold surface. The objective of this work is to study the atomistic processes responsible for plastic yield during the initial stages of indentation and explain the experimentally observed yield phenomena and defect structures.[5]

II. METHODOLOGY

The objective of this atomistic study is to investigate the defect nucleation during nanoindentation of a passivated Au(001) surface and study the mechanisms leading to plastic deformation. The atomic configuration of the system studied is illustrated in Fig. 1. The gold substrate is modeled as a slab (122 Å × 122 Å × 50 Å) containing 46400 atoms with periodic boundary conditions parallel to the surface. The orientation of the slab is such that the directions [100], [010] and [001] coincide with x, y and z. The bottom layer is fully constrained and the substrate size is sufficiently large to eliminate the finite size effects. The indenter is an assemblage of atoms in diamondoid cubic lattice arranged as a truncated pyramid with exposed (111) facets and a 15 Å × 15 Å (001) square indenting face. The indenter is oriented such that the edges of the indenting face are in [110] and [$\bar{1}$10] directions with respect to the gold crystal.

We have employed the quantum Sutton-Chen (Q-SC)[9] potential to model the gold atoms. This formulation includes the quantum corrections to better predict mechanical properties, and retains the simplicity of the original Sutton-Chen potential[10] to facilitate the understanding of the underlying physics of various processes. The indenter is modeled as a rigid body and the indenter-surface interactions are purely repulsive, $V(r) = \epsilon(r/\rho)^{-12}$ with $\epsilon = 25$ meV and $\rho =$ 3 Å , to eliminate the adhesive interactions and mimic the passivation of the gold surface in experiments.

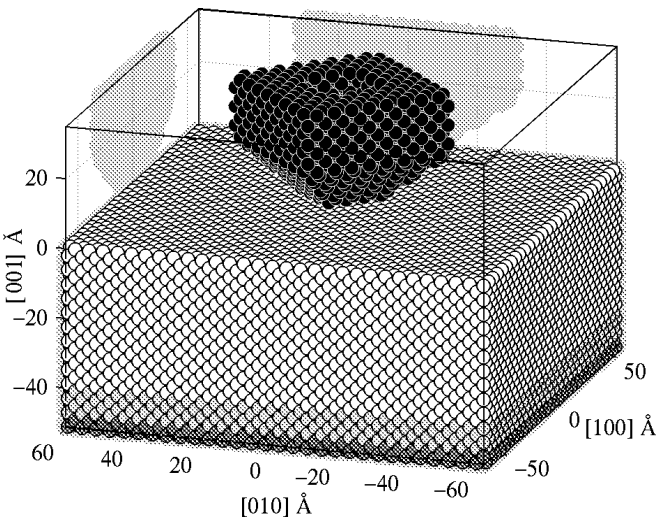


FIG. 1: Atomic configuration of the indenter and the gold substrate. ● - indenter; ○ - dynamic gold substrate; ◎ - temperature control region; ◉ - fully constrained boundary. The indenting face is a square with edges along the [110] and [$\bar{1}$10] directions of the gold crystal.

We have used an extended version of the parallel MD package DL_POLY[11] to perform the calculations. The dynamics of the substrate is evaluated by integrating the Newtonian equations of motion using Verlet-leapfrog method with a timestep of 1 fs. The gold substrate is equilibrated to its minimum energy configuration at 300 K and the indentation is simulated by advancing the indenter atoms by 0.0005 Å at every timestep, giving the indenter a velocity of 50 m/s. The temperature is regulated by periodically scaling the velocities of the atoms of the deepest non-constrained region of the substrate, away from the contact region to minimize the interference of the temperature control mechanism with the normal energy flow processes that occur in the contact region.

To understand the mechanics of plastic deformation during indentation, atomic stress tensor[12] $\boldsymbol{\sigma}$ is used to study the distribution of stresses. The von Mises shear stress, $\sqrt{J_2}$, proportional to the square root of the distortion energy, is an indicator of the onset of plastic yielding[13] as proposed by von Mises. The von Mises shear stress is given by the square root of the second invariant of the deviatoric stress, J_2, which is defined as

$$J_2 = \tfrac{1}{2}\mathrm{Tr}\left[(\boldsymbol{\sigma} - p\boldsymbol{I}) \cdot (\boldsymbol{\sigma} - p\boldsymbol{I})^{\mathrm{T}}\right], \tag{1}$$

$$p = -\tfrac{1}{3}\mathrm{Tr}(\boldsymbol{\sigma}). \tag{2}$$

where Tr denotes the trace of a matrix, $\boldsymbol{I}$ is the unit matrix and p is the local hydrostatic pressure.

In metals, plastic deformation occurs by the glide of dislocations on the slip planes. In order to identify and characterize the dislocations being nucleated during indentation we employ the slip vector analysis,[8] which provides information on the Burgers vectors of dislocations. The slip vector is defined as,

$$\boldsymbol{s} = \frac{1}{n_s}\sum_{\beta}^{n_s}\left(\boldsymbol{r}_t^{\beta} - \boldsymbol{r}_{\theta}^{\beta}\right). \tag{3}$$

where, n_s is the number of slipped neighbors β, of the reference atom, and $\boldsymbol{r}_t^{\beta}$ and $\boldsymbol{r}_{\theta}^{\beta}$ are the vector differences of atom β and the reference atom positions at times t and θ, respectively. The slip vector given by the above expression represents the Burgers vector of slip between the plane containing atom α and its adjacent atomic planes, in the time interval $[\theta, t]$. However, this is true only in the case of single slip, where the reference atom is contained by only one slip plane. In the event of multiple slip, where the atom is contained by two planes undergoing slip simultaneously, the Burgers vector is different from the slip vector given above. In any event, the slip vector will have a large magnitude for inhomogeneous, non-affine deformation near the atom and can be used to identify slipped regions.

The strains induced by indentation are studied by evaluating the atomic strain tensor as formulated by Horstemeyer and Baskes.[14] This formulation is based on the deformation gradient for a material employing many-bodied potential. The atomic Lagrangian Green strain tensor $\boldsymbol{E}$, used in this study is given by,

$$\boldsymbol{E} = \frac{1}{2}\left(\boldsymbol{F}^{\mathrm{T}}\boldsymbol{F} - \boldsymbol{I}\right), \tag{4a}$$

$$\boldsymbol{F} = \boldsymbol{X}\boldsymbol{Y}^{-1}, \tag{4b}$$

$$\boldsymbol{X} = \sum_{\beta}^{m}\left(\boldsymbol{r}_t^{\beta} \otimes \boldsymbol{r}_\theta^{\beta}\right), \tag{4c}$$

$$\boldsymbol{Y} = \sum_{\beta}^{m}\left(\boldsymbol{r}_\theta^{\beta} \otimes \boldsymbol{r}_\theta^{\beta}\right). \tag{4d}$$

where, $\boldsymbol{F}$ is the deformation gradient, m is the number of nearest neighbors β of the reference atom, $\boldsymbol{r}_\theta^{\beta}, \boldsymbol{r}_t^{\beta}$ have the same meaning as above and $\otimes$ represents tensorial product. $\boldsymbol{E}$ will then quantify the strain experienced by the reference atom in the time interval $[\theta, t]$.

To investigate the mechanisms of dislocation nucleation and glide on the slip planes, we study the resolved shear stresses on the slip planes along the Burgers vectors given by the slip vector analysis. The resolved shear stress τ on a plane with normal $\hat{\boldsymbol{n}}$ along the direction of slip $\hat{\boldsymbol{b}}$ is given by,

$$\tau_{(\boldsymbol{n})[\boldsymbol{b}]} = \hat{\boldsymbol{b}} \cdot \boldsymbol{\sigma} \cdot \hat{\boldsymbol{n}} \tag{5}$$

Schmid law[15] states that a slip system is activated when the resolved shear stress on that system reaches a critical value called the critical resolved shear stress (CRSS).

III. RESULTS AND DISCUSSION

A. Indentation

The force versus displacement curve for the initial stages of indentation is shown in Fig. 2. The force F_z is calculated as the sum total of the forces exerted on the indenter atoms by the substrate and the displacement z_{sep} is the separation between the indenter apex and the surface of the substrate before indentation. Initially, the force curve displays elastic behavior until the force decreases abruptly at the first yield point, marked as (**1**) in Fig. 2. This phenomenon is associated with the nucleation of a plastic event to partially relieve the elastic stress in the contact region. This observation is in excellent agreement with other theoretical[7,8,16,17,18] and experimental results.[4,5,6] Upon further indentation the force begins to rise again, displaying yet another region of elastic behavior, until the substrate undergoes a second yield event (**2**) in Fig. 2. It is interesting to see that the force curve has a higher slope in the second elastic response region and the second yield occurs at a higher force. This is indicative of strain hardening at the atomic scale resulting in an increase in the yield modulus and strength.

1. First Yield : Defect Nucleation

To gain insight into this behavior, the evolution of the stress profiles in the contact region during indentation are analyzed. Figures 3 and 4 show the von Mises shear stress $\sqrt{J_2}$ and hydrostatic pressure p profiles in the region directly beneath the indenter at various stages of indentation marked $(a) - (d)$ in Fig. 2. Figures 3(a), (b) and 4(a), (b) show that as the indentation proceeds from (a) to (b), an increase in $\sqrt{J_2}$, a measure of the elastic stored energy, substantiates the elastic response seen in the force curve in this regime. At point (b) the elastic stress reach a threshold beyond which plastic deformation occurs that partially relieves and dissipates the elastic energy from the surface as seen in 3(c). This behavior is in accordance with the von Mises criterion,[13] which suggests a critical value for $\sqrt{J_2}$ for the onset of plastic activity. Upon further indentation from (c) to (d) $\sqrt{J_2}$ increases again implying another elastic response regime, which culminates in the second yield event.

To study the nature of plastic deformation and characterize the defect structures nucleated, the deformed regions are identified by the slip vector $\boldsymbol{s}_{01}$, where **0** represents the initial undeformed state and **1** represents the state after the first yield event. Three snapshots of the deformed region at various stages of defect nucleation between (b) and (c) are shown in Fig. 5 to illustrate the evolution of the defect structure. From the slipped atoms shown in Fig. 5 it is seen that dislocation loops nucleate on the four {111} planes at the surface and extend into the solid. These dislocation

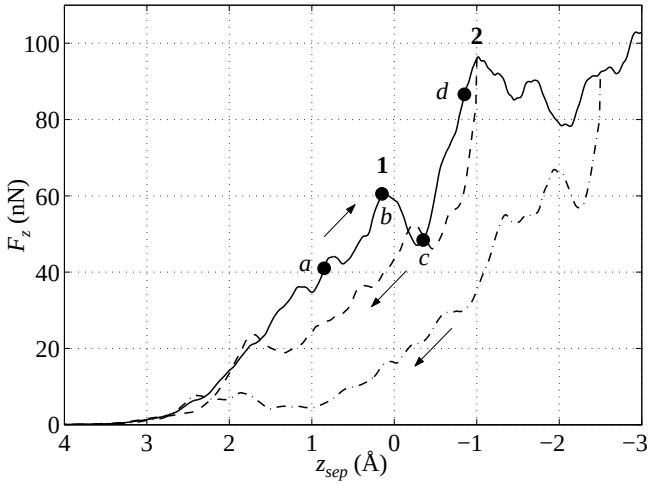


FIG. 2: Force versus distance curve during initial stages of indentation. $(a)-(b)$ elastic response; (b) onset of first yield; $(b)-(c)$ first plastic yield event; $(c)-(d)$ second elastic response at a higher force and with a higher slope indicating strain hardening. **1** and **2** represent the first and second yield events.

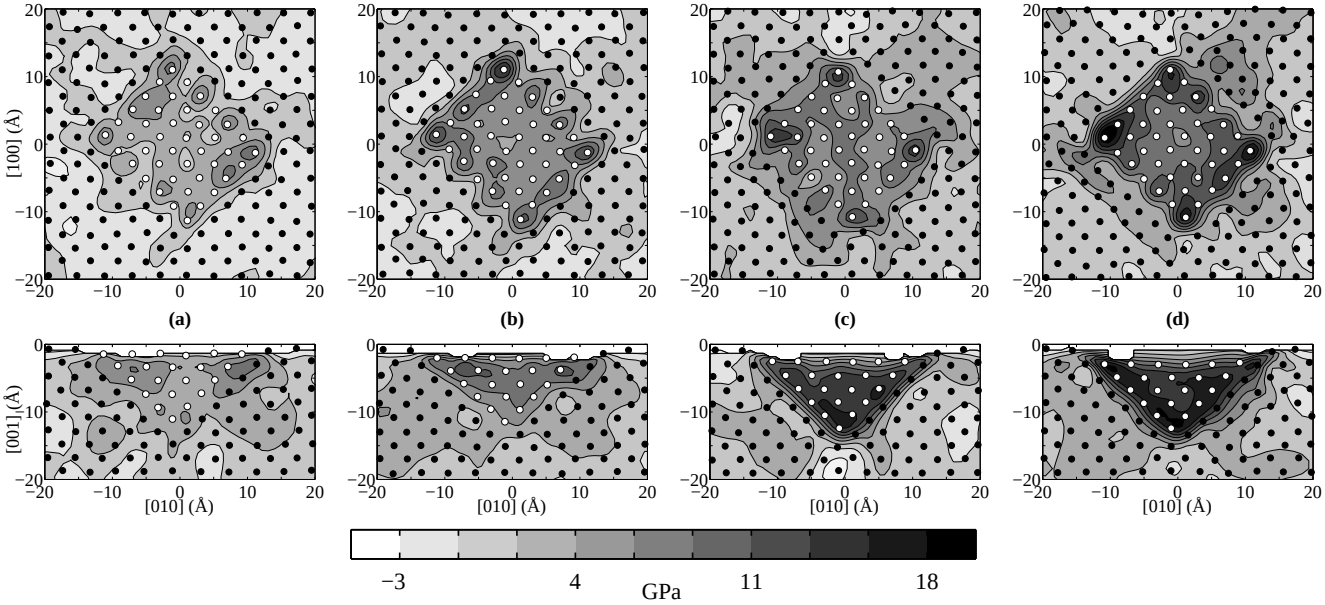


FIG. 3: Contour plots of the atomic von Mises shear stress $\sqrt{J_2}$ in the indented region at four stages of indentation marked $(a)-(d)$ in Fig. 2. The contours are on [001] surface (upper row) just beneath the indenter and [100] surface (lower row) at $x = 0$. ○ are the slipped atoms that comprise the defect nucleated during the first yield event and ● are the undeformed atoms. Stress is concentrated at the corners of the contact region. Increase in $\sqrt{J_2}$ from (a) to (b) and (c) to (d) signifies elastic responses and a drop from (b) to (c) indicates plastic yield.

loops grow in size and intersect with the loops on the adjacent planes forming a pyramidal defect structure as seen in Fig. 5(c). Figure 6 shows the corresponding slip vectors of the atoms on one of the slip planes, (111). From Fig. 6(c) the magnitude of the slip vector of the atoms on the (111) plane is close to 1.66 Å along $[11\bar{2}]$, which is consistent with the $\langle 112 \rangle$ partial dislocations on $\{111\}$ planes in gold. The dislocation nucleated on the (111) plane is therefore the $\frac{1}{6}[11\bar{2}]$ Shockley partial, and similarly $\frac{1}{6}[\bar{1}1\bar{2}]$, $\frac{1}{6}[1\bar{1}\bar{2}]$ and $\frac{1}{6}[\bar{1}\bar{1}\bar{2}]$, partials are nucleated on $(\bar{1}11)$, $(1\bar{1}1)$ and $(\bar{1}\bar{1}\bar{1})$ planes, respectively. Thus the defect consists of intersecting intrinsic stacking faults on the four $\{111\}$ planes, which intersect the (001) surface with four fold symmetry. This pyramidal defect structure is in excellent agreement with

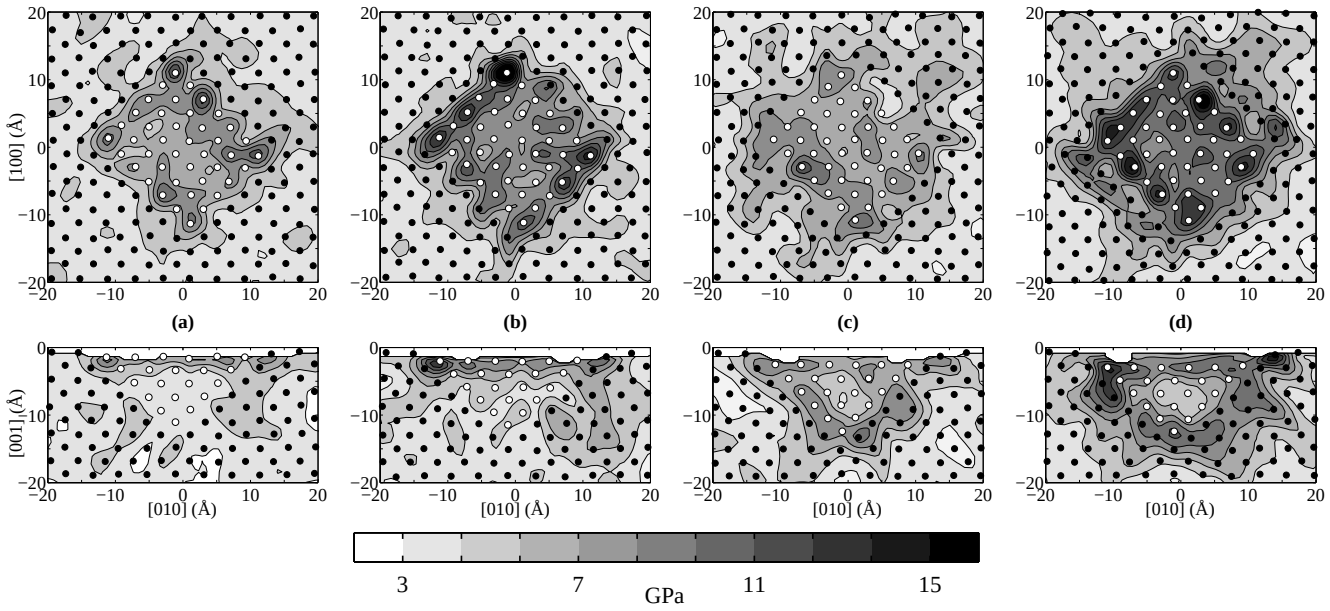


FIG. 4: Contour plots of the atomic hydrostatic pressure p in the indented region at four stages of indentation marked $(a)-(d)$ in Fig. 2. The contours are on [001] surface (upper row) just beneath the indenter and [100] surface (lower row) at $x = 0$. ○ are the slipped atoms that comprise the defect nucleated during the first yield event and ● are the undeformed atoms. Stress is concentrated at the corners of the contact region. After the first yield (c), a compressive strain of 0.052 in the defect gives rise to increased pressure of the order of $10-15$ GPa.

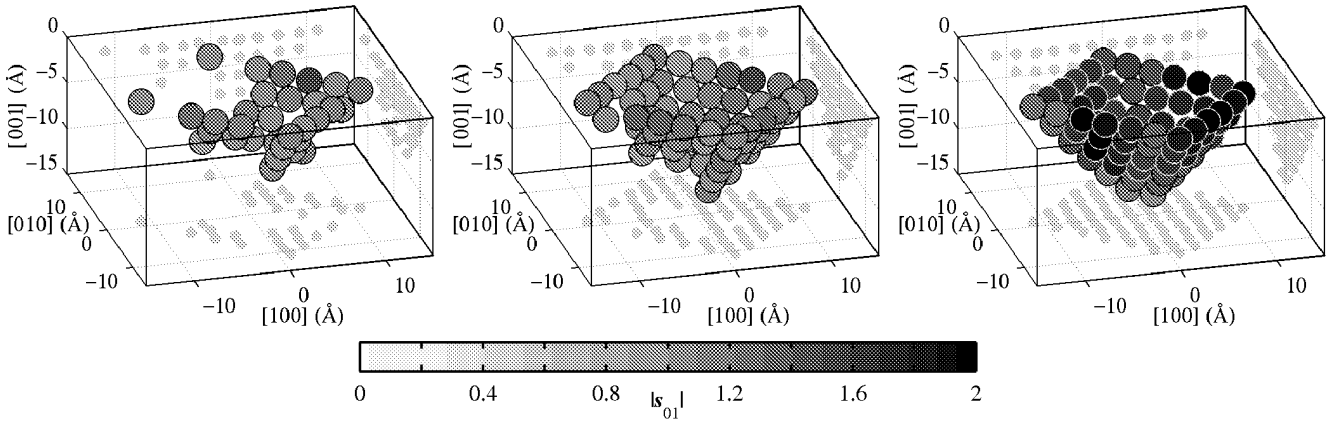


FIG. 5: Snapshots of deformed region depicting the evolution of the dislocation structures nucleated during the first yield event $((b)-(c)$ in Fig. 2). Greyscale represents $|\boldsymbol{s}_{01}|$.

the experimentally observed permanent deformation structures.[5]

From continuum elastic theory[19] of indentation by a rigid flat frictionless punch, similar to the atomic indenter used in this study, the stresses reach a theoretically infinite value at the edges of the indenter. This observation, at the atomic scale, is validated by the large concentrations of stresses at the periphery of the contact region as seen in Figs. 3(b) and 4(b), in agreement with previous studies.[16,18] Surface nucleation of partial dislocations in areas of enhanced stress is well supported experimentally[20,21] and theoretical models of surface dislocation nucleation at stress concentrators[22,23,24,25] are well established. The corners of the contact region act as stress concentrators and serve as the sources of nucleation of Shockley partials on the surface. Under the influence of the stresses, these partials glide on the $\{111\}$ planes, the dominant slip planes in gold, forming intrinsic stacking faults as seen in Fig. 6. This slip results in the flow of part of the elastic energy from the contact surface to the sheared surfaces and is seen as an increase in $\sqrt{J_2}$ in the region of slip in Fig. 3(c). The strain undergone by the atoms in the deformed region during defect nucleation is quantified by the mean Lagrangian strain tensor in Voigt notation, $\boldsymbol{E} = \begin{bmatrix} 0.068 & 0.064 & -0.166 & 0.007 & -0.002 & 0.02 \end{bmatrix}$.

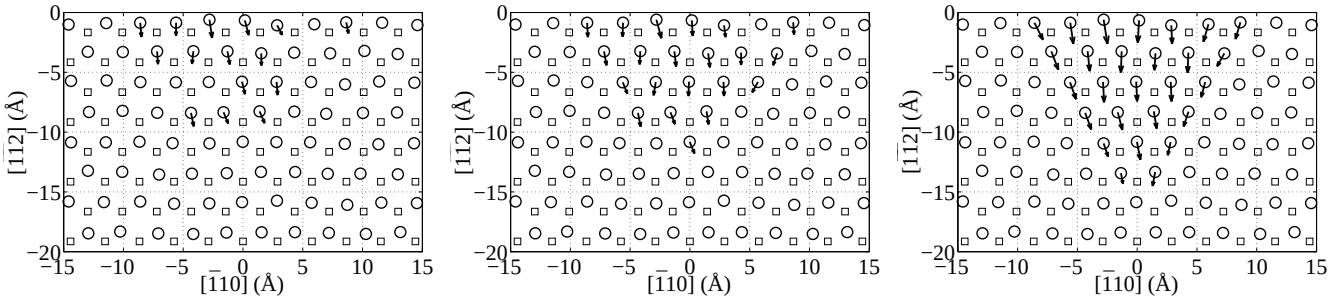


FIG. 6: Slip vector ($\boldsymbol{s}_{01}$) maps on (111) plane corresponding to the snapshots in Fig. 5. ○ represent the atoms of the slipped plane and □ represent the atoms of the unslipped plane adjacent to the slipped region.

Thus the observed strain is in $\langle 100 \rangle$ directions and gives a volumetric strain of -0.052 in the pyramidal defect, giving rise to higher pressures of the order of $10 - 15$ GPa (with a bulk modulus of 207 GPa) above the ambient pressures as seen in Fig. 4(c).

In order to understand why this particular slip system $\{111\}\langle 11\bar{2} \rangle$ has been activated, we study the resolved shear stresses (RSS), as the direction of slip has been associated with maximum RSS. Fig. 8 shows the distribution of $\tau_{(111)[10\bar{1}]}$, $\tau_{(111)[01\bar{1}]}$ and $\tau_{(111)[11\bar{2}]}$ on the (111) slip plane along $[10\bar{1}]$, $[01\bar{1}]$ and $[11\bar{2}]$, respectively. These are the favored slip directions[26] on (111) plane for the current stress state ($\boldsymbol{\sigma} \approx \sigma_{zz}$). It is seen that even though $\tau_{(111)[10\bar{1}]}$ and $\tau_{(111)[01\bar{1}]}$ have higher concentrations near the surface than $\tau_{(111)[11\bar{2}]}$, the slip occurs along $[11\bar{2}]$. This incongruency of slip occurring in a lower RSS direction is consistent with the findings of other researchers[8] and can be explained by the concept of generalized stacking fault energy (GSF) γ, introduced by Vitek.[27,28] GSF is the energy per unit area of a fault plane created by the rigid slip of one half of a perfect lattice relative to the other along a slip plane in a general slip direction. Fig. 7 shows the unrelaxed GSF in the dominant slip directions [110] and [112].

The maximum value of γ in the direction of slip, called the unstable stacking energy γ_{us},[29] is the energy barrier to be overcome during slip. It is seen from Fig. 7 that γ_{us} displays a strong directional dependence and slip along [112] has a lower energy barrier than [110] and is thus more favorable as observed in this study. However, γ is a static quantity and is not an appropriate measure to describe the dynamics of slip. A better quantity would be the theoretical shear stress required to initiate and maintain the slip along the slip direction. This shear stress is given by

$$\tau^{th}_{\{\boldsymbol{n}\}\langle \boldsymbol{r} \rangle} = \frac{\partial \gamma_{\boldsymbol{n}}}{\partial \boldsymbol{r}} \tag{6}$$

where, $\gamma_{\boldsymbol{n}}$ is the GSF on a slip plane with normal $\boldsymbol{n}$ and $\boldsymbol{r}$ is the displacement vector. A plot of this stress for slip on $\{111\}$ plane along $\langle 110 \rangle$ and $\langle 112 \rangle$ directions is shown in Fig. 7. The maximum value of τ^{th} is the resolved shear stress that is required to complete the slip along the particular direction. This is the critical resolved shear stress (CRSS) τ^c referred to in Schmid law[15] as stated above. From Figs. 7 and 8 $\tau^c_{\{111\}\langle 112 \rangle}$ is 2.34 GPa and is smaller than the observed $\tau_{(111)[11\bar{2}]}$ values. On the other hand $\tau^c_{\{111\}\langle 110 \rangle}$ has a value of 8.88 GPa and is much higher than the observed $\tau_{(111)[11\bar{2}]}$ values. Thus, the observed slip direction is $[11\bar{2}]$ rather than $[01\bar{1}]$ or $[10\bar{1}]$. Second and higher derivatives of γ could be used to further refine the dynamics of slip, but it is beyond the scope of this paper and for the present study τ would suffice.

The smallest of the directionally dependent τ^c represents the ideal shear strength of the crystal is 2.34 GPa in excellent agreement with the experimental estimates of 1.5 to 2.0 GPa.[4,5] The high τ values of 5 GPa, in Fig. 8, greater than the theoretical estimate of the ideal shear strength might seem out of order, but it needs to be clarified that the theoretical value is based on a block like shear and such instantaneous rigid slip cannot be expected during the actual nucleation and propagation of slip. These τ values are also quite high compared to the experimental CRSS because the values in Fig. 8 are highly localized and are inaccessible to experimental investigations. The shear stress values deduced from experiments represent the mean value of the shear stresses in the region local to indentation and a plot of such a mean of τ is shown in Fig. 9. It can be seen that these values reach a maximum and drop abruptly at the first yield point validating the manifestation of Schmid law at the atomic scale. The maximum RSS on (111) is along $[11\bar{2}]$ and reaches a value of 1.95 GPa and on the other $\{111\}$ planes the maximum RSS are in the range of 1.8 to 2.3 GPa. These values agree exceptionally well with the experimental estimates of 2 GPa.

The plastic strains produced by indentation are complex and activation of multiple slip systems is necessary to accommodate these general yields.[30] Groves and Kelly[31] have predicted the active slip systems by calculating the strain produced by a given slip system[32] and identifying the systems that contribute to the observed strain. Such

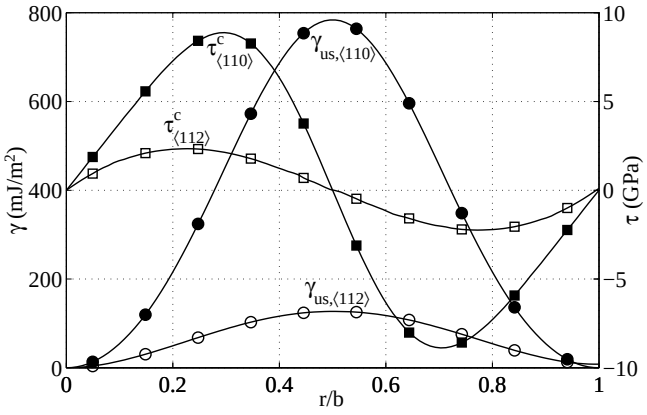


FIG. 7: Generalized stacking fault energies γ (circles) and theoretical shear stresses τ^{th} (squares) for slip systems $\{111\}\langle 112\rangle$ (open) and $\{111\}\langle 110\rangle$ (solid). Lower $\tau^c_{\langle 112\rangle}$ indicates a more energetically favorable $\{111\}\langle 112\rangle$ slip system.

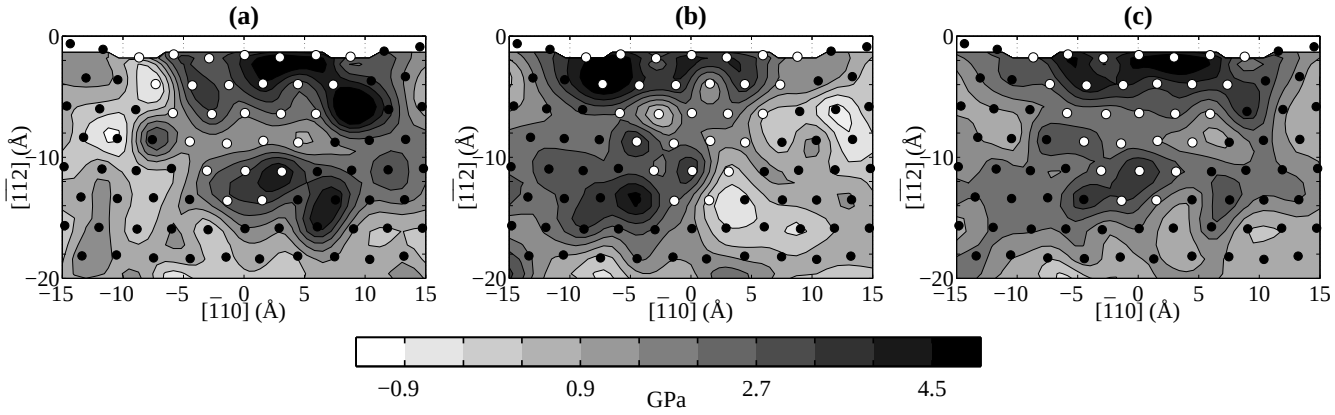


FIG. 8: Resolved shear stresses on (111) plane, just before the first yield point, along favored directions of slip: (a) $[01\bar{1}]$; (b) $[10\bar{1}]$; (c) $[11\bar{2}]$. ○ are the slipped atoms that constitute the stacking fault and ● are the atoms in the undeformed region. In some regions $\tau_{(111)[11\bar{2}]}$ is smaller than $\tau_{(111)[10\bar{1}]}$ and $\tau_{(111)[01\bar{1}]}$.

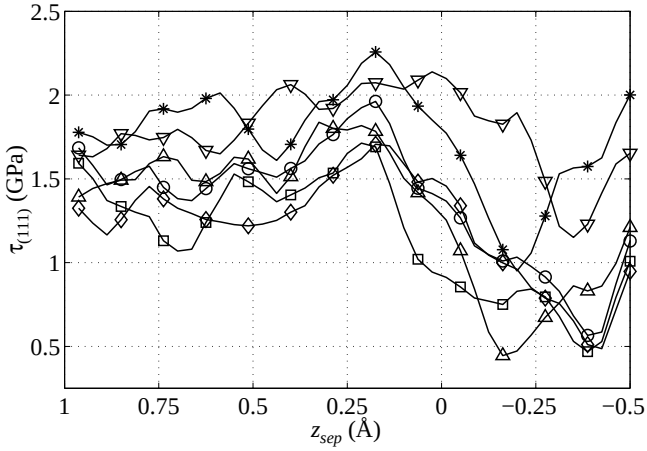


FIG. 9: Mean resolved shear stresses in the deformed region for slip systems: □ $(111)[01\bar{1}]$; ◇ $(111)[10\bar{1}]$; ○ $(111)[11\bar{2}]$; ∗ $(\bar{1}11)[\bar{1}1\bar{2}]$; ▽ $(1\bar{1}1)[1\bar{1}\bar{2}]$; △ $(\bar{1}\bar{1}1)[\bar{1}\bar{1}\bar{2}]$. The resolved shear stresses reach a threshold at the yield point. The maximum resolved shear stress is in the range of $1.8 - 2.3$ GPa.

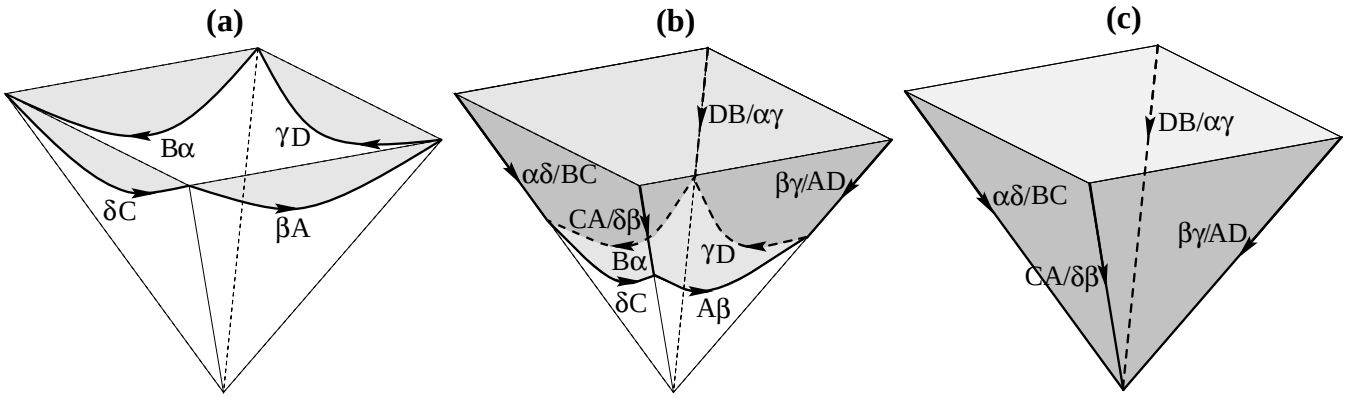


FIG. 10: Various stages in the formation of the pyramidal defect structure. Shaded regions represent intrinsic stacking faults. (a) nucleation and glide of partials; (b) dislocation loop growth and zipping resulting in sessile stair-rods; (c) pyramidal defect structure.

a geometrical analysis[33] for compression in [001], which is the observed stress state just before the first yield point, predicts activation of slip on the four {111} planes resulting in plastic strains in ⟨100⟩. These predicted slip planes and strains are identical to those observed at the atomic scale in this study.

In the event of the presence of multiple sets of independent slip systems capable of producing the required strain, as is the case with f.c.c. crystals, Bishop and Hill[34,35] proposed a stress criterion for yielding that requires the attainment of CRSS on the active slip systems, without exceeding CRSS on the inactive systems. The observed slip directions conform to the above criterion with the shear stresses reaching their critical values in ⟨112⟩, but not in ⟨110⟩.

2. Defect Nucleation Mechanism

Based on the results and discussion presented above, we propose a three step mechanism for the formation of the pyramidal defect during indentation of Au (001). It is convenient for the following discussion to use Thompson's notation for Burgers vectors and planes and refer to Fig. 10 for an illustration of the mechanism.

Dislocation nucleation: Surface indentation of Au (001) with an indenter results in large concentration of stresses at the corners of the contact region. These stress concentrators, where the RSS on the {111} planes reach the CRSS, act as the sources for surface nucleation of Shockley partials ($\frac{1}{6}\langle 11\bar{2}\rangle$) B$\alpha$, A$\beta$, γD and δC on the slip planes $(\bar{a}), (\bar{b}), (c)$ and (d) respectively.

Dislocation glide: These partials, under the influence of the external stress due to indentation, glide away from the surface forming intrinsic faults on the slip planes.

Dislocation reaction: As the dislocation loops grow, the partials attract each other in pairs and zip to form sessile stair-rods along AC, AD, BD and BC according to the following reactions:

$$\begin{aligned} \delta\mathrm{C} + \beta\mathrm{A} &= \delta\beta/\mathrm{CA} \\ \mathrm{A}\beta + \mathrm{D}\gamma &= \mathrm{AD}/\beta\gamma \\ \gamma\mathrm{D} + \alpha\mathrm{B} &= \gamma\alpha/\mathrm{DB} \\ \mathrm{B}\alpha + \mathrm{C}\delta &= \mathrm{BC}/\alpha\delta \end{aligned} \tag{7}$$

In vector notation the energetically favorable reactions are of the type

$$\tfrac{1}{6}[11\bar{2}] - \tfrac{1}{6}[\bar{1}1\bar{2}] = \tfrac{1}{3}[100] \tag{8}$$

The final defect, therefore, consists of a pyramid of intrinsic stacking faults on {111} planes, which intersect the (001) surface with a four fold symmetry, and the $\langle 01\bar{1}\rangle$ edges of the pyramid consist of low energy sessile stair-rod dislocations. These sessile stair-rods act as barriers to further glide giving rise to the observed strain hardening during indentation beyond the first yield.

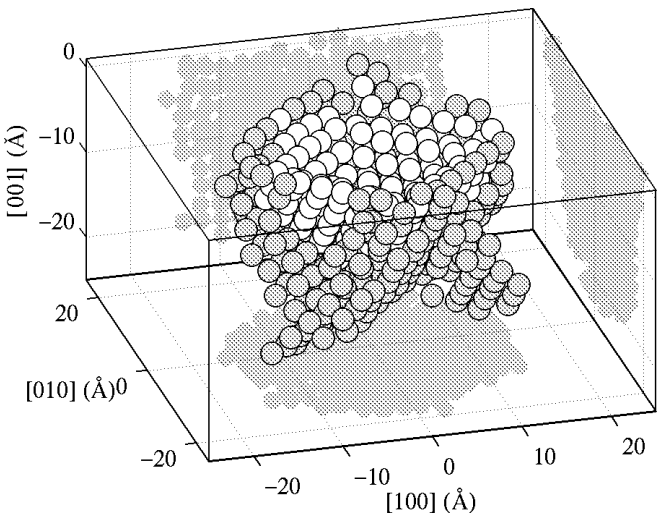


FIG. 11: Deformed region illustrating the dislocation locks formed during the second yield. ○ represent the atoms that slipped during the first yield ($|\boldsymbol{s}_{01}| > 0$) and ● are the atoms that underwent slip during the second yield event ($|\boldsymbol{s}_{12}| > 0$). Dislocation loops extend beyond the adjacent faces of defect structure forming dislocation locks.

To examine the dependence of the defect structures on the orientation of the indenter with respect to the crystallographic axes of the gold substrate, the calculations were repeated with the edges of the indenting face in (100) and (010) directions. The defect produced was similar to the pyramidal structure seen above where the high stresses at the corners of contact region nucleate partials on the four {111} planes. From the physics of the defect nucleation presented above, the above mechanism can be generalized to indentation of other {111} and {110} surfaces as well. It can be deduced that the indentation of {111} surface will produce a tetrahedral defect structure displaying the three-fold symmetry observed in experiments.[5] And similarly the hexagonal nature of the indent produced by indenting the {110} surface is consistent with the proposed mechanism. Thus, the geometry of the defect structures is independent of the indenter orientation, but is a characteristic of the crystallography of the surface of the indented crystal.

3. Second Yield : Dislocation Locks

Further indentation results in a second yield, at which point dislocation loops are nucleated on the slip planes outside the defect as shown in Fig. 11. Figure 12 shows the slip vectors $\boldsymbol{s}_{12}$, of the atoms on the (111) plane dislocated during the second yield and the dislocation loops extending beyond the stair-rods can be seen. The contour plots of RSS on (111)⟨112⟩ along with the slip vectors are shown in Fig. 13. It is seen that the activated slip direction is not along the maximum RSS direction, but along the direction in which the RSS has reached the critical value. This observation further corroborates the discussion presented above. Thus, deformation results through a sequence of elastic and plastic responses, with the elastic responses culminating in plastic events.

B. Retraction

When the indenter is retracted after the first yield point, the force curve retraces the indentation path at small displacements. This suggests that the defect nucleated at the first yield point has disappeared and the substrate has recovered is original undeformed state upon retraction. However, the force curve during retraction after the second yield point signifies permanent deformation.

Upon retracting the indenter, the external stress vanishes and the internal compressive stress dominates the dynamics of deformation. It is seen above that the interior of the pyramidal defect is under enormous compressive stress due to the strain imposed during the first yield. This compressive stress when resolved onto the slip planes is opposite in direction to the RSS during indentation. A restoring force is induced that is strong enough to effect the unzipping of the stair-rods into their constituent partials, which then glide toward the surface healing the stacking

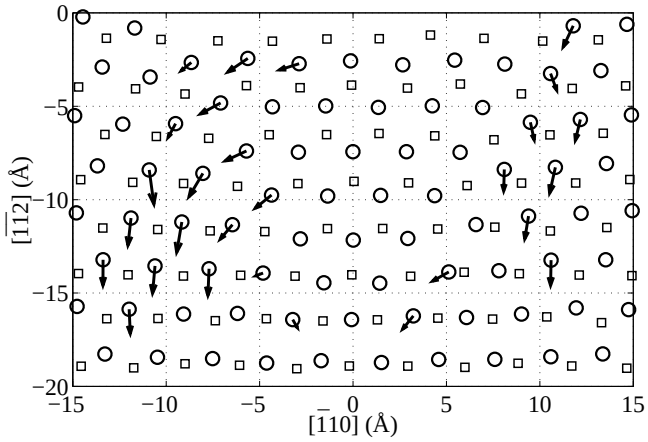


FIG. 12: Slip vector $\boldsymbol{s}_{12}$ of the atoms on (111) plane. ○ represent the atoms of the slipped plane and □ represent the atoms of the unslipped plane adjacent to the slipped region. The slip is along the direction in which the resolved shear stress has attained the critical value.

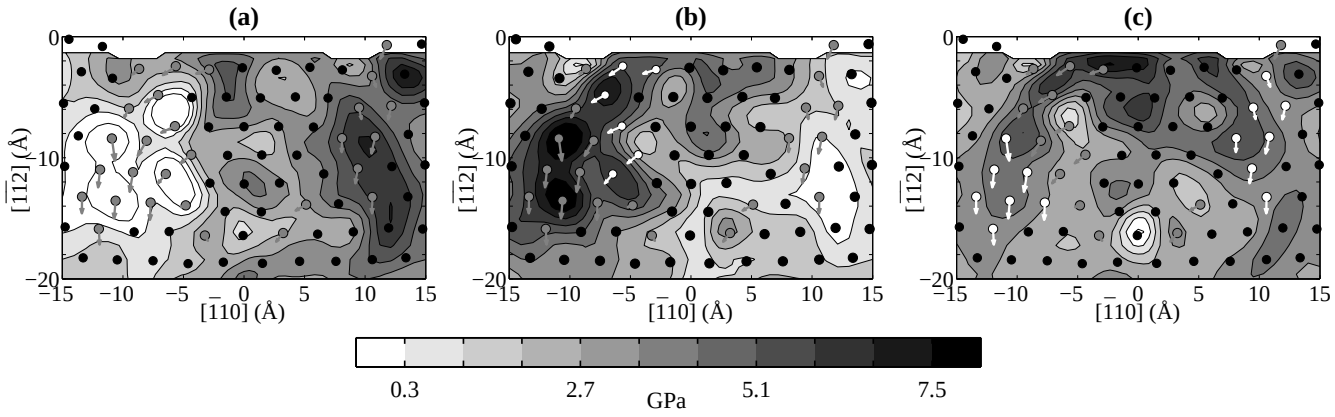


FIG. 13: Resolved shear stresses on (111) plane, at the second yield point, along the direction: (a) $[12\bar{1}]$; (b) $[21\bar{1}]$; (c) $[11\bar{2}]$. ○ represent the atoms with slip vectors coinciding with the RSS direction; ● represent other slipped atoms and ● represent the atoms in the undeformed region. The observed slip is not necessarily in direction of the maximum resolved shear stress.

fault along the way. Eventually, the defect disappears and the substrate recovers its original configuration with no residual deformation as seen in Fig. 2.

However, after the second yield, the dislocation loops extend beyond the stair-rods leading to dislocation locking. And upon retracting the indenter after the second yield, the aforementioned restoring forces are not strong enough to unlock the locked structure, thus giving rise to permanent plastic deformation observed in Fig. 2.

IV. CONCLUDING REMARKS

We have investigated the atomistic mechanisms of plastic deformation during nanoindentation of Au (001) surface with a noninteracting indenter. A recently developed slip vector analysis has been employed to identify the defect structures formed during initial plastic yield. During indentation, the accumulated elastic energy in the indented region is partially relieved by the nucleation of a pyramidal defect structure. The defect is formed by the surface nucleation of Shockley partials on the four {111} slip planes at the periphery of the contact region. These partials glide away from the surface creating stacking faults that grow in size and intersect with those on the adjacent planes. At the intersections, the partials zip to form sessile stair-rods which contribute to the strain hardening observed after the first yield. The observed slip is in the most energetically favorable direction, which corresponds to the direction in which the RSS has reached the critical value and is not necessarily the maximum value. The CRSS estimated in

this study is in the range of $1.8 - 2.3$ GPa in excellent agreement with the experimental estimates.

Upon retracting the indenter after the first yield, the pressure due to the compressive strain in the defect induces restoring forces that heal the plastic deformation. Further indentation results in a second yield that causes the dislocation loops to extend beyond the stair-rods forming dislocation locks. The unlocking forces of these structures is greater than the internal restoring forces active during indenter retraction and thus effect permanent deformation after the second yield.

We proposed a three step mechanism based on dislocation theory that elucidates the physics behind the formation of the observed defect structures during gold nanoindentation. According to this mechanism, the defects produced depend on the crystallography of the indented surface as seen in experiments.

V. ACKNOWLEDGMENTS

This work was supported by NSF Career Grant BES-9983735. The calculations were performed using parallel computing resources of High Performance Computing Partnership at Iowa State University.

---

* Electronic address: suryakm@iastate.edu

[1] S. Mader, A. Seeger, and H. M. Thieringer, J. Appl. Phys. **34**, 3376 (1963).
[2] M. S. Whelan, in *The Physics of Metals: Defects*, edited by P. B. Hirsch (Cambridge University, London, 1975), vol. 2, p. 98.
[3] R. A. Wind, M. J. Murtagh, F. Mei, Y. Wang, M. A. Hines, and S. L. Sass, Appl. Phys. Lett **78**, 2205 (2001).
[4] S. G. Corcoran, R. J. Colton, E. T. Lilleodden, and W. W. Gerberich, Phys. Rev. B **55**, R16057 (1997).
[5] J. D. Kiely and J. E. Houston, Phys. Rev. B **57**, 12588 (1998).
[6] J. D. Kiely, K. F. Jarausch, J. E. Houston, and P. E. Russell, J. Mater. Res. **14**, 2219 (1999).
[7] C. L. Kelchner, S. J. Plimpton, and J. C. Hamilton, Phys. Rev. B **58**, 11085 (1998).
[8] J. A. Zimmerman, C. L. Kelchner, P. A. Klein, J. C. Hamilton, and S. M. Foiles, Phys. Rev. Lett. **87**, 165507 (2001).
[9] Y. Kimura, Y. Qi, T. Çağin, and W. A. Goddard III (1998), unpublished.
[10] A. P. Sutton and J. Chen, Philos. Mag. Lett. **61**, 139 (1990).
[11] W. Smith and T. R. Forester, *DL_POLY is a package of molecular simulation routines* (1996), © The Council for the Central Laboratory of the Research Councils, Daresbury Laboratory at Daresbury, Nr, Warrington.
[12] T. Egami and J. Srolovitz, J. Phys-Paris **12**, 2141 (1982).
[13] G. Dieter, *Mechanical Metallurgy* (McGraw-Hill, New York, 1967).
[14] M. F. Horstemeyer and M. I. Baskes, in *Multiscale Phenomena in Materials - Experiments and Modeling*, edited by I. M. Robertson, D. H. Lassila, B. Devincre, and R. Phillips (Materials Research Society, Pennsylvania, 2000), vol. 578 of *Materials Research Society Symposium Proceedings*, p. 15.
[15] E. Schmid and W. Boas, *Crystal Plasticity* (Hughes and Co. Ltd., London, 1950).
[16] U. Landman, W. D. Luedtke, N. A. Burnham, and R. J. Colton, Science **248**, 454 (1990).
[17] A. Buldum, S. Ciraci, and I. P. Batra, Phys. Rev. B **57**, 2468 (1998).
[18] A. Gannepalli and S. K. Mallapragada, Nanotechnology **12**, 250 (2001).
[19] K. L. Johnson, *Contact Mechanics* (Cambridge University Press, Cambridge, 1985).
[20] X. J. Ning and N. Huvey, Phil. Mag. A **74**, 241 (1996).
[21] J. Doerschel, Z. Kristallogr. **209**, 210 (1994).
[22] S. V. Kamat and J. P. Hirth, J. Appl. Phys. **67**, 6844 (1990).
[23] H. Gao, J. Mech. Phys. Solids **42**, 741 (1994).
[24] G. E. Beltz and L. B. Freund, in *Thin Films: Stresses and Mechanical Properties V*, edited by S. P. Baker, P. Borgesen, P. H. Townsend, C. A. Ross, and C. A. Volkert (Materials Research Society, Pennsylvania, 1995), vol. 356 of *Materials Research Society Symposium Proceedings*, p. 93.
[25] J. Zou and J. H. Cockayne, J. Appl. Phys. **79**, 7632 (1996).
[26] The Schmid factors for $\boldsymbol{\sigma} = \sigma_{zz}$ on (111) along $[10\bar{1}]$, $[01\bar{1}]$ and $[11\bar{2}]$ are 0.4082, 0.4082 and 0.4714 respectively.
[27] V. Vitek, Phil. Mag. **18**, 773 (1968).
[28] V. Vitek, L. Lejcek, and D. K. Bowen, in *Interatomic Potentials and Simulation of Lattice Defects*, edited by P. C. Gehlen, J. R. Beeler Jr, and R. L. Jaffee (Plenum Press, New York, 1972), p. 493.
[29] J. R. Rice, J. Mech. Phys. Solids **40**, 239 (1992).
[30] R. von Mises, Z. angew. Math. Mech. **8**, 161 (1928).
[31] G. W. Groves and A. Kelly, Phil. Mag. **8**, 877 (1963).
[32] J. F. W. Bishop, Phil. Mag. **42**, 414 (1953).
[33] C. N. Reid, *Deformation Geometry for Materials Scientists*, vol. 11 of *International Series on Materials Science and Technology* (Pergamon Press, Oxford, 1973).
[34] J. F. W. Bishop and R. Hill, Phil. Mag. **42**, 414 (1951).
[35] J. F. W. Bishop and R. Hill, Phil. Mag. **42**, 1298 (1951).